





Loss of glymphatic homeostasis in heart failure

 Marios Kritsilis,^{1,2} Lotte Vanherle,^{1,2,3} Marko Rosenholm,^{4,5,6} René in 't Zandt,⁷ Yuan Yao,⁸ Kelley M. Swanberg,^{1,2} Pia Weikop,⁴ Michael Gottschalk,⁷ Nagesh C. Shanbhag,^{1,2} Jiebo Luo,⁸ Kimberly Boster,⁹ Maiken Nedergaard,^{4,10}
 Anja Meissner^{1,2,3} and Iben Lundgaard^{1,2}

See Harrison (<https://doi.org/10.1093/brain/awaf054>) for a scientific commentary on this article.

Heart failure is associated with progressive reduction in cerebral blood flow and neurodegenerative changes leading to cognitive decline. The glymphatic system is crucial for the brain's waste removal, and its dysfunction is linked to neurodegeneration.

In this study, we used a mouse model of heart failure, induced by myocardial infarction, to investigate the effects of heart failure with reduced ejection fraction on the brain's glymphatic function.

Using dynamic contrast-enhanced MRI and high-resolution fluorescence microscopy, we found increased solute influx from the CSF spaces to the brain, i.e. glymphatic influx, at 12 weeks post-myocardial infarction. Two-photon microscopy revealed that cerebral arterial pulsatility, a major driver of the glymphatic system, was potentiated at this time point, and could explain this increase in glymphatic influx. However, clearance of proteins from the brain parenchyma did not increase proportionately with influx, while a relative increase in brain parenchyma volume was found at 12 weeks post-myocardial infarction, suggesting dysregulation of brain fluid dynamics. Additionally, our results showed a correlation between brain clearance and cerebral blood flow.

These findings highlight the role of cerebral blood flow as a key regulator of the glymphatic system, suggesting its involvement in the development of brain disorders associated with reduced cerebral blood flow. This study paves the way for future investigations into the effects of cardiovascular diseases on the brain's clearance mechanisms, which may provide novel insights into the prevention and treatment of cognitive decline.

1 Department of Experimental Medical Science, Lund University, 22362 Lund, Sweden

2 Wallenberg Center for Molecular Medicine, Lund University, 22184 Lund, Sweden

3 Department of Physiology, Institute of Theoretical Medicine, University of Augsburg, 86159 Augsburg, Germany

4 Center for Translational Neuromedicine, Faculty of Medical and Health Sciences, University of Copenhagen, 2200 Copenhagen, Denmark

5 Division of Pharmacology and Pharmacotherapy, Faculty of Pharmacy, University of Helsinki, 00014 Helsinki, Finland

6 Individualized Drug Therapy Research Program, Faculty of Medicine, University of Helsinki, 00014 Helsinki, Finland

7 Lund University Bioimaging Centre, Lund University, 22184 Lund, Sweden

8 Department of Computer Science, University of Rochester, Rochester, NY 14627, USA

9 Department of Mechanical Engineering, University of Rochester, Rochester, NY 14627, USA

10 Center for Translational Neuromedicine, University of Rochester Medical School, Rochester, NY 14642, USA

Received August 20, 2024. Revised November 04, 2024. Accepted December 03, 2024. Advance access publication December 18, 2024

© The Author(s) 2024. Published by Oxford University Press on behalf of the Guarantors of Brain.

This is an Open Access article distributed under the terms of the Creative Commons Attribution-NonCommercial License (<https://creativecommons.org/licenses/by-nc/4.0/>), which permits non-commercial re-use, distribution, and reproduction in any medium, provided the original work is properly cited. For commercial re-use, please contact reprints@oup.com for reprints and translation rights for reprints. All other permissions can be obtained through our RightsLink service via the Permissions link on the article page on our site—for further information please contact journals.permissions@oup.com.

Correspondence to: Iben Lundgaard
 Department of Experimental Medical Science, Lund University, BMC A1304b, Sölvegatan 19, 22362 Lund, Sweden
 E-mail: iben.lundgaard@med.lu.se

Keywords: cerebrospinal fluid; cardiovascular disease; cerebral blood flow

Introduction

Heart failure is a progressive and potentially fatal condition that affects >10% of people over 65 years of age, a prevalence expected to increase in the following decades.¹ It is characterized by impaired cardiac function and dysfunction in multiple organs, including the brain.² Heart failure is associated with cognitive decline and has been identified as a risk factor for Alzheimer's disease.^{3–6} Diverse processes, including cerebral hypoperfusion, chronic inflammation and subsequently protein aggregation, may be involved in the association between heart failure and cognitive decline, but causative mechanisms thereof remain unclear.^{2,7,8}

The glymphatic system is considered to be the extracellular waste clearance system of the brain and is characterized by the transport of CSF from the peri-arterial space into the brain parenchyma.⁹ This exchange between CSF and interstitial fluid (ISF) is facilitated by the water channel aquaporin-4 (AQP4), which is highly expressed on the astrocytic endfeet that form the outer wall of the perivascular space (PVS).^{10,11} The ISF then disperses towards the perivenous and perineuronal spaces and ultimately exits the CNS along perineural sheaths of cranial and spinal nerves, meningeal lymphatic vessels, parasagittal dura and arachnoid granulations.^{12–17} Cerebral arterial pulsations are considered a major driver of this CSF glymphatic influx,^{18,19} while vascular pathologies, such as arterial stiffening, have been reported to impede it.^{19–21} Impairment of the glymphatic system and, therefore, incomplete clearance of protein aggregates from the brain, may lead to neurodegeneration and Alzheimer's disease,^{22,23} processes associated with heart failure.^{3,24} We therefore investigated whether the glymphatic system is impaired in heart failure and what the mechanisms underlying this interaction may be.

Materials and methods

Animals

Three-month-old male wild-type C57BL/6N mice were purchased from Taconic Biosciences. Animals were housed in a climate-controlled facility under a standard 12-h:12-h light-dark cycle, in groups of three to five in individually ventilated cages with environmental enrichment, fed normal chow and given access to food and water *ad libitum*. Upon arrival, animals were acclimatized for at least 5 days before any handling or experimental procedure was initiated. Experiments performed in Lund were approved by the Malmö-Lund ethical Committee on Animal Research (5.2.18–10 992/18, 5.8.18–14 734/2021, 5.8.18–20 240/2021 and V 2023/1245). Experiments performed at the Center for Translational Neuromedicine at the University of Copenhagen were approved by the Danish Animal Inspectorate and by the Department of Animal Experimental Medicine of the University of Copenhagen (2020-15-0201-00562).

Induction of myocardial infarction

Myocardial infarction (MI) was induced by surgical ligation of the left anterior descending (LAD) coronary artery as previously

described.²⁵ Details of the MI induction surgery can be found in [Supplementary material, 'Methods' section](#).

MRI hardware and acquisition parameters

All MRI acquisitions were done on a 9.4 T preclinical magnetic resonance scanner using an Agilent magnet (Agilent), Bruker BioSpec Avance III electronics (Bruker), actively shielded gradients with integrated shims (BGA 12S HP, Bruker; maximum strength 670 mT/m; rise time 130 μ s) and operated via ParaVision 7.0.0. The following sequences were used:

For cardiac MRI, a modified Bruker 2D ultra-short echo time (UTE)²⁶ imaging sequence [echo time = 0.5 ms; repetition time = 5 ms; slice thickness = 1 mm; matrix size 96 \times 96; field of view (FOV) = 25 \times 25 mm²; flip angle α = 7°] was used to acquire a total of 12 064 spokes per slice within 1 min. To measure brain volume, high-resolution T₂-weighted rapid acquisition by refocused echoes (RARE; echo time = 21.4; repetition time = 3550 ms; slice thickness 0.5 mm; 30 slices; 120 \times 150; resolution 0.5 \times 0.5 mm²; α = 180°; echo train length 8; number of averages N_A = 13) acquisitions were used. For regional cerebral blood flow (CBF) measurements, flow-sensitive alternating inversion recovery echo-planar imaging (FAIR-EPI; echo time = 13.27 ms; repetition time = 2039.8 ms; spectral bandwidth 320.175 kHz; slice thickness 1.5 mm; image matrix 73 \times 64; resolution 0.2344 \times 0.2329 mm²; N_A = 4) acquisitions with global presaturation over six inversion times for slice-selective and global inversion conditions were localized to coronal slices in the striatum and hippocampus, respectively. For dynamic contrast-enhanced (DCE)-MRI experiments, the 3D fast low-angle shot (FLASH) sequence (echo time = 1.5 ms; repetition time = 10 ms; α 10°; 100 μ m isotropic resolution; acquisition time 2.5 min per time point) was used.

Complete details of image acquisitions, processing and analysis can be found in the [Supplementary material, 'Methods' section](#).

Cisterna magna injection and vasculature labelling

Mice were anaesthetized with an intraperitoneal (i.p.) injection of K/X (ketamine 100 mg/kg/xylazine 20 mg/kg), administered in a volume of 10 ml/kg and after losing the toe pinch reflex, each mouse was placed on a small animal physiological monitoring device connected to a head fixation frame (Harvard Apparatus). The cisterna magna (CM) was revealed by making an incision and reflecting the muscles overlying the back of the skull, as previously described.²⁷ Complete details of CM injection and vasculature labelling can be found in [Supplementary material, 'Methods' section](#).

Intraparenchymal tracer injection

For the intraparenchymal injection of fluorescent tracer, mice were anaesthetized with isoflurane (2.5%–3% induction in O₂, 1.5–2% maintenance in O₂, 0.8–1 l/min) and placed on a stereotactic frame. Body temperature was kept stable using a heating pad. The skin over the dorsal skull was locally anaesthetized with bupivacaine (Marcaïn® 5 mg/ml, Aspen Nordics) before being opened, and a burr hole was drilled on the coordinates: AP +0.6 mm; ml

–2.0 mm, relative to bregma. A glass capillary containing the fluorescent tracer Alexa Fluor™ 647 conjugated bovine serum albumin (BSA-647, 67 kDa, 10 mg/ml, diluted in artificial CSF, A34785, Invitrogen/Thermo Fisher Scientific) connected to a 10 µl Hamilton syringe (Hamilton Company) was slowly inserted at DV –3.3 mm from the skull. Tracer (1 µl) was injected at a rate of 0.2 µl/min. To avoid backflow, the capillary was left in place for 10 min after the injection. The capillary was then slowly retracted and the incision was closed using surgical glue (Histoacryl®, B. Braun Medical AB) and bupivacaine was applied subcutaneously to the wound area. The mice were allowed to recover in a heated cage until they woke up from the anaesthesia. Forty-eight hours after the injection, the mice were anaesthetized with K/X and transcardially perfused with PBS and 4% paraformaldehyde (PFA). The brains were then immersion-fixed overnight in 4% PFA before further analysis.

Preparation of cranial window

Mice were anaesthetized with isoflurane (induction: 4% in O₂, maintenance: 2% in O₂, 0.8–1 l/min), placed on a rodent heating pad to maintain body temperature at 36°C–37.5°C, and fixed to a stereotactic frame. After losing the toe pinch reflex, the head of the mouse was shaved and cleaned with isopropyl alcohol. Mice were administered lidocaine (Lidocain Accord, 1 mg/kg, subcutaneously) at the incision site as a local anaesthetic and carprofen (Rimadyl Vet, Zoetis, 5 mg/kg, i.p.) for postoperative analgesia. A piece of the skin from the scalp was cut (~1.3 cm diameter) to expose the animals' skull, and the surface of the skull was cleaned and dried. An aluminium frame was attached to the skull of the mice using dental acrylic (Fuji LUTE BC, GC and Super Bond, Sun Medical). To maximize transparency through the optical window, craniotomy was chosen over skull-thinning. A 4 mm diameter craniotomy was performed using a dental drill centred above the barrel-field cortex ~2.5 mm posterior to bregma. To prevent overheating, ice-cold artificial CSF was continuously perfused over the skull while drilling. When sufficiently thinned, the bone was gently removed and a thin circular 4-mm diameter glass coverslip was mounted in its place. The coverslip was fixed to the skull with dental cement (C&B Metabond®, Parkell). Animals were allowed to recover for a minimum of 2 days before two-photon imaging. The mice were administered carprofen (5 mg/kg, i.p.) once every 24 h for 2 days after the surgery.

In vivo two-photon imaging of arterial pulsatility

Animals were imaged under a two-photon microscope (Thorlabs Bergamo with a Spectra Physics InSight® DS+™ laser) using a 25× objective (25× Nikon CFI APO LWD Objective, 380–1050 nm, 1.10 NA, 2.0 mm WD). Images were acquired using ThorImage®LS v3.0 software. Complete details of two-photon imaging and arterial pulsatility and vasomotion analysis can be found in [Supplementary material, 'Methods' section](#).

Ex vivo fluorescence imaging

Following transcardial perfusion and overnight fixation in 4% PFA, brains injected with BSA-647 were imaged from both dorsal and ventral surfaces using a Nikon SMZ25 stereomicroscope with a Plan Apo 0.5× objective (0.08 NA, ×0.5 magnification) equipped with an Andor Zyla VSC-04095 camera. The exposure time was 40 ms for the dorsal and 30 ms for the ventral brain images. For

the analysis of glymphatic influx, a region of interest was drawn around the cerebral cortex and olfactory bulbs, and mean fluorescence intensities were analysed using Fiji²⁸ and used as a measure of CSF tracer influx. Due to the proximity of the cerebellum and pons to the injection site and because of potential damage to these structures during brain isolation, these regions were excluded from the *ex vivo* analysis.

Brain clearing and light-sheet microscopy

To optically clear the brains, the immunolabelling-enabled 3D imaging of solvent-cleared organs (iDISCO+) protocol was carried out, as previously described.²⁹ Complete details of brain clearing and light-sheet microscopy can be found in the [Supplementary material, 'Methods' section](#).

Immunohistochemistry

Brains fixed in 4% PFA were cut into 100 µm thick sections using a Leica V1200S vibratome (Leica Biosystems) and brain sections were used for AQP4, collagen IV and laminin immunostaining. Complete details of immunohistochemistry protocols, brain section imaging and analysis can be found in the [Supplementary material, 'Methods' section](#).

Plasma norepinephrine analysis

Before transcardial perfusion, heart blood was collected from mice in sterile EDTA-coated 1.5 ml centrifuge tubes. The blood was then centrifuged at 1000g for 10 min at 4°C. The plasma supernatant was separated, snap frozen and stored at –80°C until used for analysis of norepinephrine by high-performance liquid chromatography with electrochemical detection, as previously described.³⁰

Statistical analysis

All statistical analyses were performed using GraphPad Prism 10 (GraphPad Software, San Diego, CA, USA). Data were tested for normality using the Shapiro-Wilk test. When comparing two groups, two-tailed unpaired Student's *t*-test or Mann-Whitney test was used. Variances were compared using an *F*-test, and the unpaired two-tailed Welch's *t*-test was used in cases of unequal variance. In cases wherein comparisons between the two groups were made for different time points or brain regions, *P*-values were adjusted for multiple comparisons using the Holm-Sidak method. For signal enhancement over time measurements, the two-tailed repeated measures two-way ANOVA with the Geisser-Greenhouse correction was used. The *P*-value reported for these represents the *P*-value of the comparison between the Time × Group linear model coefficients, given that there is a significant difference between both the time and group coefficients separately. Pearson correlation was used to assess the relationship between variables that were normally distributed. For variables that did not meet the normality assumption, Spearman correlation was used instead. The statistical tests performed for each dataset along with the test statistic, degrees of freedom and number of animals (*n*) are stated in the corresponding figure legends. *P* < 0.05 was considered significant for rejection of the null hypothesis.

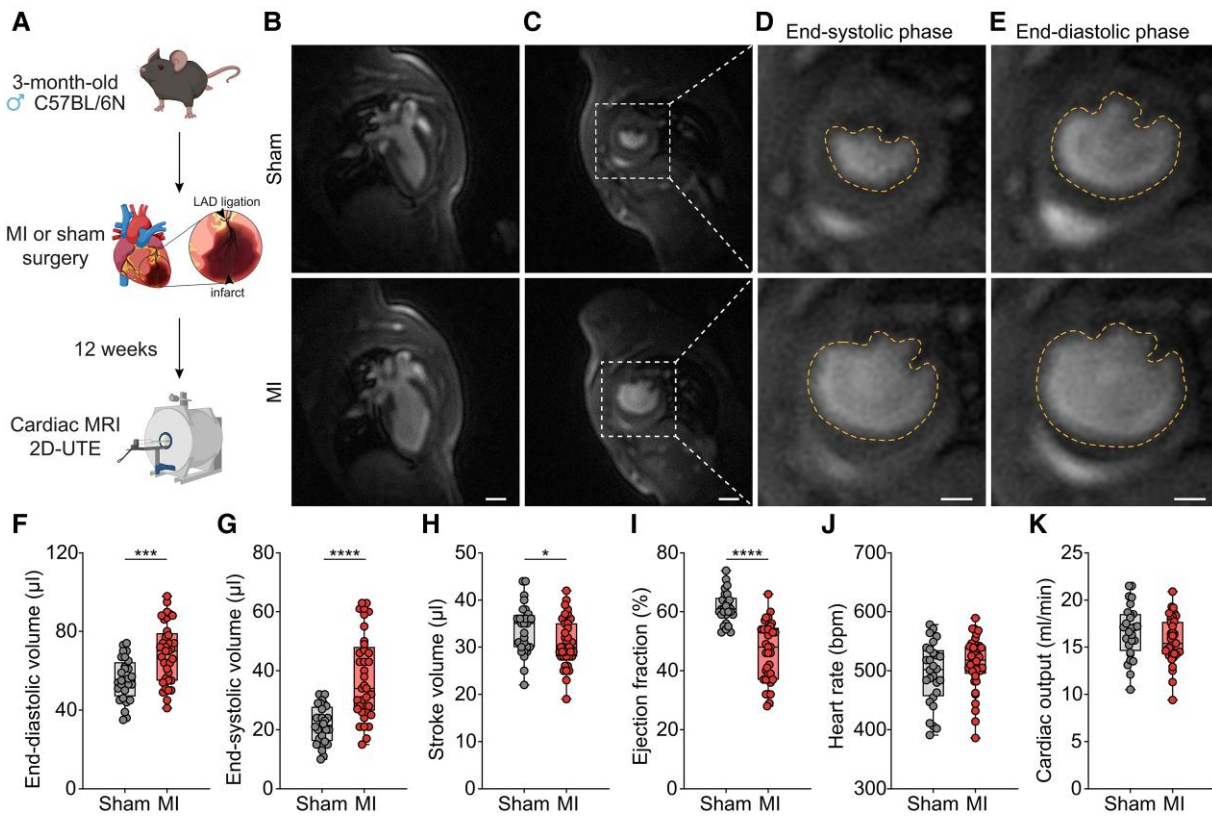


Figure 1 Systolic dysfunction of the left ventricle following myocardial infarction. (A) Schematic representation of the experiment. Three-month-old male C57BL/6N mice underwent either myocardial infarction (MI) or sham surgery [inset highlights the left anterior descending (LAD) artery ligation and infarct] and 12 weeks post-surgery, their left ventricular function was assessed using a 2D-UTE MRI sequence. (B–E) Representative slice images from a sham (top) and a MI (bottom) mouse cardiac scan showing the long axis view of the left ventricle (B), the short axis view of the left ventricle (LV) at the end-systolic phase (C) and the magnified short axis views of the left ventricle at the end-systolic (D) and the end-diastolic phase (E) (LV volume marked with yellow dashed line). (F) LV end-diastolic volume at 12 weeks post-MI or sham surgery [unpaired two-tailed Welch's *t*-test, $t(63) = 3.904$, $P = 0.0002$, $n = 28$ sham, $n = 37$ MI]. (G) LV end-systolic volume at 12 weeks post-MI or sham surgery [unpaired two-tailed Welch's *t*-test, $t(52.46) = 6.146$, $P < 0.0001$, $n = 28$ sham, $n = 37$ MI]. (H) LV stroke volume at 12 weeks post-MI or sham surgery [unpaired two-tailed Student's *t*-test, $t(63) = 2.282$, $P = 0.0259$, $n = 28$ sham, $n = 37$ MI]. (I) LV ejection fraction at 12 weeks post-MI or sham surgery [unpaired two-tailed Welch's *t*-test, $t(57.13) = 7.786$, $P < 0.0001$, $n = 28$ sham, $n = 37$ MI]. (J) Heart rate at 12 weeks post-MI or sham surgery (two-tailed Mann-Whitney test, $U = 414$, $P = 0.1704$, $n = 28$ sham, $n = 37$ MI). (K) Cardiac output at 12 weeks post-MI or sham surgery [unpaired two-tailed Student's *t*-test, $t(63) = 1.531$, $P = 0.1308$, $n = 28$ sham, $n = 37$ MI]. Scale bars in B and C = 2 mm; D and E = 1 mm. Box plots represent median, quartiles, min and max values, with individual animals shown as coloured dots. * $P < 0.05$, *** $P < 0.001$, **** $P < 0.0001$. 2D-UTE = two-dimensional ultrashort echo time.

Results

Myocardial infarction causes systolic dysfunction, but the cardiac output is preserved

We used a mouse model of heart failure with reduced ejection fraction (HFrEF), induced by LAD coronary artery ligation, mimicking MI. Cardiac function was evaluated using MRI at 3, 6 or 12 weeks post-MI or sham surgery (Fig. 1A). The left ventricle (LV) at the 12-week time point showed an apparent enlargement in MI mice compared to the sham controls both at the end-systolic and the end-diastolic phase of the cardiac cycle (Fig. 1B–E). Quantification of the left ventricular volumes revealed a significant increase in the end-diastolic and end-systolic volumes in the MI mice, which was evident at all time points (Fig. 1F and G and Supplementary Fig. 1A, B, G and H). While stroke volume was decreased only at the 12-week time point (Fig. 1H and Supplementary Fig. 1C and I), ejection fraction (EF) was consistently decreased at all time points (Fig. 1I and Supplementary Fig. 1D and J). Interestingly, the heart rate and cardiac output did not differ between MI and sham mice throughout disease progression (Fig. 1J and K and Supplementary

Fig. 1E, F, K and L). These results show that systolic dysfunction occurs at an early stage in this model of HFrEF without necessarily compromising cardiac output, and are in line with previous work using this model.²⁵

Increased glymphatic influx at 12 weeks post-myocardial infarction

Glymphatic influx at 12 weeks post-MI or sham surgery was assessed by injecting fluorescent tracer BSA-647 in the CM. Following 30 min of tracer circulation, mice were transcatheterially perfused and CSF tracer influx at dorsal and ventral brain surfaces were measured after overnight fixation (Fig. 2A). Surprisingly, we observed increased glymphatic influx in MI relative to sham mice more prominently in ventral brain (Fig. 2B–F), while mean fluorescence intensity in the ventral brain showed an inverse correlation with EF in these mice (Fig. 2F). To enable observation of whole-brain tracer distribution, brains were optically cleared using the iDISCO+ protocol²⁹ and imaged with light-sheet microscopy (Fig. 2A). Analysis of total brain tracer reflected the previous results, although no statistically significant difference was found between

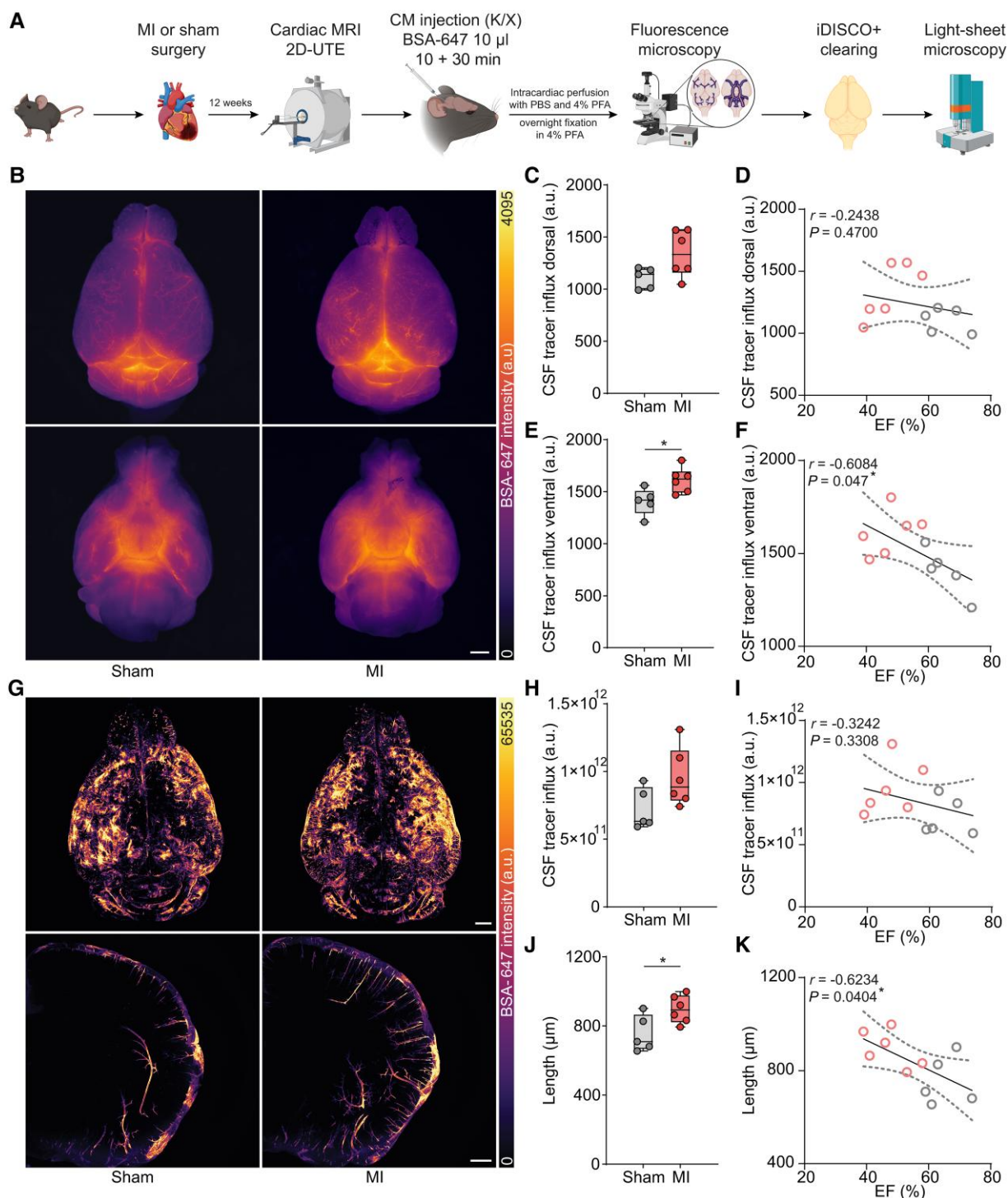


Figure 2 Heart failure increases CSF tracer distribution in the brain at 12 weeks post-myocardial infarction. (A) Schematic representation of the experimental timeline. (B) Representative images of CSF tracer distribution at the dorsal (top) and ventral (bottom) brain surfaces from a sham and a myocardial infarction (MI) mouse. (C) Quantification of mean fluorescence intensity of CSF tracer influx at the dorsal brain surface [unpaired two-tailed Student's *t*-test, $t(9) = 2.169$, $P = 0.0582$, $n = 5$ sham, $n = 6$ MI]. (D) Correlation between ejection fraction and mean fluorescence intensity at the dorsal brain surface (Pearson's correlation, $r = -0.2438$, $R^2 = 0.05944$, $P = 0.4700$, $n = 11$). (E) Quantification of mean fluorescence intensity of CSF tracer influx at the ventral brain surface [unpaired two-tailed Student's *t*-test, $t(9) = 2.771$, $P = 0.0217$, $n = 5$ sham, $n = 6$ MI]. (F) Correlation between ejection fraction and mean fluorescence intensity at the ventral brain surface (Pearson's correlation, $r = -0.6084$, $R^2 = 0.3702$, $P = 0.047$, $n = 11$). (G) Representative 3D reconstructed images of fluorescent tracer influx in the optically cleared whole brain, dorsal view (top) and maximum projection of a 500-µm thick coronal section around bregma (bottom). (H) Quantification of sum fluorescence intensity of CSF tracer influx at the optically cleared whole brain [unpaired two-tailed Student's *t*-test, $t(9) = 2.021$, $P = 0.074$, $n = 5$ sham, $n = 6$ MI]. (I) Correlation between ejection fraction and sum fluorescence intensity of CSF tracer influx at the optically cleared whole brain (Pearson's correlation, $r = -0.3242$, $R^2 = 0.1051$, $P = 0.3308$, $n = 11$). (J) Quantification of average length of vessels with perivascular influx at the dorsolateral cortex [unpaired two-tailed Student's *t*-test, $t(9) = 2.545$, $P = 0.0315$, $n = 5$ sham, $n = 6$ MI]. (K) Correlation

(Continued)

the groups (Fig. 2G and H) and this measure did not correlate with EF (Fig. 2I). We then measured the depth of tracer penetration along the dorsolateral penetrating vessels of cleared brains (Fig. 2G). An increased tracer penetration depth was observed in MI mice versus sham (Fig. 2J), which also correlated with reduced EF (Fig. 2K). These results indicate that HFrEF leads to increased glymphatic influx at 12 weeks post-MI.

Gradual increase in glymphatic influx during HFrEF progression

We further investigated glymphatic dynamics *in vivo* and at different time points during HFrEF progression. Mice subjected to MI or sham surgery were injected with a gadolinium-based contrast agent (GBCA) in the CM at 3, 6 or 12 weeks after surgery (Fig. 3A and Supplementary Figs 2A and 3A). Glymphatic transport was tracked *in vivo* using a DCE-MRI protocol consisting of two baseline scans, four time points during GBCA infusion and 20 more time points during GBCA circulation for a total time of ~65 min (Fig. 3B and Supplementary Figs 2B and 3B). To quantify glymphatic influx in the brain, volumes of interest (VOIs) were placed similarly to Stanton et al.³¹ at the ventral brain surface at the level of the anterior cerebral artery and the hypothalamus and 1 mm dorsally (Fig. 3C and L and Supplementary Figs 2C and L and 3C and L). At 3 weeks post-surgery, signal enhancement in the brain parenchyma showed similar temporal dynamics between MI and sham in all VOIs (Supplementary Fig. 2D, H, M and Q). Accordingly, the area under the curve (AUC) of the signal enhancement and the peak enhancement did not differ between the groups at this time point (Supplementary Fig. 2E, F, I, J, N, O, R and S), and did not correlate with the EF, despite it being reduced in MI mice (Supplementary Fig. 2G, K, P and T). At 6 weeks post-MI, we found a subtle but consistent increase in glymphatic influx dynamics compared to sham in the ventral hypothalamus (Supplementary Fig. 3D, H, M and Q). Similarly, AUC and peak enhancement were increased in MI mice in some but not all VOIs (Supplementary Fig. 3E, F, I, J, N, O, R and S). An inverse correlation was found between the AUC at the ventral VOIs and EF (Supplementary Fig. 3G and P), which was not present at the more dorsal VOIs (Supplementary Fig. 3K and T). As heart failure further progressed at 12 weeks post-MI induction, comparison of glymphatic influx dynamics revealed a significant increase in MI compared to sham at all analysed VOIs (Fig. 3D, H, M and Q). AUC and peak enhancement were also significantly increased in MI versus sham (Fig. 3E, F, I, J, N, O, R and S) and again only ventral VOI AUC correlated with EF (Fig. 3G, K, P and T). Comparing the differences between the AUC means at the different time points revealed that glymphatic influx notably increased from 3 to 6 weeks and then remained elevated at similar levels at 12 weeks post-MI. Taken together, these findings confirm that HFrEF causes a delayed increase in glymphatic influx, which is proportionate to the EF reduction.

Nasal CSF efflux is not affected by HFrEF

Following CM injection, solute tracer is thought to partially exit the cranium via multiple CSF efflux routes.³² One important

such route is the nasal pathway, where CSF exits the subarachnoid space along the olfactory neurons that pass through the cribriform plate towards the nasal mucosa, eventually reaching the cervical lymphatic vessels.^{14,33,34} To examine whether the increased glymphatic influx that was observed 12 weeks post-MI was influenced by downstream effects, such as reductions in CSF drainage, DCE-MRI measurements were used to measure signal enhancement over time in the nasal turbinates. Within manually segmented nasal region masks, a multi-step threshold was applied to isolate nasal turbinate tissue and analysis was limited to voxels that significantly enhanced following contrast injection (Fig. 4A). The dynamics of the CSF efflux through the nasal turbinates did not differ between MI and sham (Fig. 4B and C). Accordingly, there was no difference in enhancement AUC and peak enhancement between the two groups (Fig. 4D and E), while these measures did not correlate with EF (Fig. 4F and G). These data suggest that increased glymphatic influx is unlikely due to reduced nasal efflux of CSF to the periphery.

Increased cerebral arterial pulsatility at 12 weeks post-MI

Cerebral arterial pulsatility and slow vasomotion have a central role in driving glymphatic flow.^{18,19,35,36} To test whether these mechanisms are responsible for the increased glymphatic influx in heart failure, FITC-dextran was retro-orbitally injected to visualize the cerebral vasculature and pial arteries were imaged using two-photon microscopy, during both wakefulness and K/X anaesthesia (Fig. 5A and B). During wakefulness, arterial pulsatility and slow vasomotion did not differ between MI and sham mice at 12 weeks post-surgery (Fig. 5C and D). Under K/X anaesthesia, arterial pulsatility (Fig. 5E) but not slow vasomotion (Fig. 5F), was significantly increased in MI mice compared to sham, revealing a plausible mechanism for the increased glymphatic influx that was observed in HFrEF. While arterial pulsatility during the awake state correlated with that under K/X anaesthesia (Fig. 5G), the increase in MI relative to sham was significant only in the latter case. Following two-photon imaging, mice were injected with fluorescent BSA-647 in the CM. After 30 min of tracer circulation, the mice were retro-orbitally injected with WGA-488 for vasculature labelling, followed by transcatheter perfusion and brain isolation (Fig. 5A). Confocal imaging of brain sections was used to visualize the width of the PVS, stained with BSA-647, relative to the width of the vessels, stained with WGA-488 lectin³⁷ (Fig. 5H). Quantification of the PVS index between MI and sham mice did not reveal any significant difference (Fig. 5I). Plasma norepinephrine levels were also not significantly different between the groups at this time point (Fig. 5J). Taken together, these data suggest that HFrEF leads to increased glymphatic influx by enhancing arterial pulsatility.

HFrEF does not affect AQP4 polarization, extracellular matrix proteins and blood–brain barrier permeability

The water channel AQP4 and especially its polarized expression at the astrocytic endfeet, have central roles in glymphatic influx and clearance.^{9,10,38} To investigate whether heart failure affects AQP4

Figure 2 Continued

between ejection fraction and average length of vessels with perivascular influx (Pearson's correlation, $r = -0.6234$, $R^2 = 0.3887$, $P = 0.0404$, $n = 11$). Scale bars in B = 2 mm; G = 1 mm (top), 500 μm (bottom). Colour map: B and G = inferno. Box plots represent median, quartiles, min and max values, with individual animals shown as coloured dots. Individual animals are represented as coloured circles in the correlation graphs, red (MI) and grey (sham). * $P < 0.05$. 2D-UTE = two-dimensional ultrashort echo time; CM = cisterna magna; EF = ejection fraction; iDISCO = immunolabelling-enabled 3D imaging of solvent-cleared organs; K/X = ketamine/xylazine; PFA = paraformaldehyde.

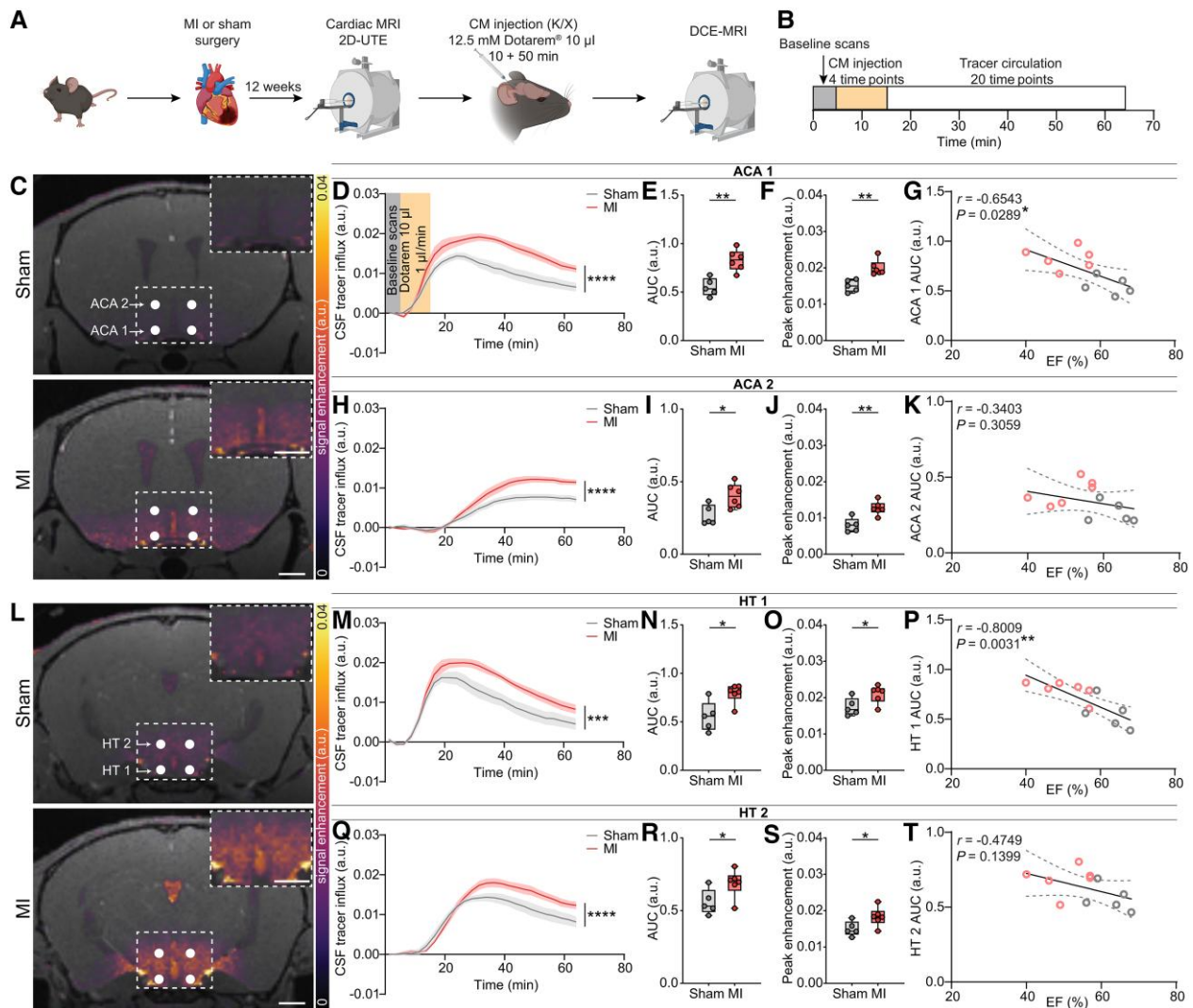


Figure 3 Heart failure leads to increased glymphatic influx at ventral brain regions after 12 weeks post-myocardial infarction. (A) Schematic representation of the experimental timeline. (B) Overview of DCE-MRI protocol consisting of two baseline measurements, followed by four time points during the injection of 10 µl of Dotarem® in the cisterna magna (CM) at a rate of 1 µl/min and 20 more time points of CSF contrast agent circulation. (C) Representative coronal images of parenchymal contrast agent infiltration 20 min after the end of the CM injection, at the level of the anterior cerebral artery (ACA) from a sham (top) and a myocardial infarction (MI) (bottom) mouse. Signal enhancement was quantified by parenchymal volumes of interest (VOIs, white circles) positioned right above the ACA (ACA 1) and 1 mm dorsally (ACA 2). Insets highlight the CSF tracer influx at the ventral brain area. (D–G) Characteristics of the CSF tracer influx at the ACA 1 VOI, including the time – mean enhancement curve [two-tailed repeated measures two-way ANOVA, Time × Group: $F(25,225) = 3.587, P < 0.0001$; Time: $F(1.926,17.33) = 66.04, P < 0.0001$; Group: $F(1,9) = 19.94, P = 0.0016, n = 5$ sham, $n = 6$ MI] (D), the area under the curve (AUC) [unpaired two-tailed Student’s *t*-test, $t(9) = 4.515, P = 0.0015, n = 5$ sham, $n = 6$ MI] (E), the peak enhancement [unpaired two-tailed Student’s *t*-test, $t(9) = 4.174, P = 0.0024, n = 5$ sham, $n = 6$ MI] (F) and the correlation between the AUC and the ejection fraction (EF) (Pearson’s correlation, $r = -0.6543, R^2 = 0.4282, P = 0.0289, n = 11$) (G). (H–K) Characteristics of the CSF tracer influx at the ACA 2 VOI, including the time – mean enhancement curve [two-tailed repeated measures two-way ANOVA, Time × Group: $F(25,225) = 7.096, P < 0.0001$; Time: $F(2.439,21.95) = 139.5, P < 0.0001$; Group: $F(1,9) = 7.956, P = 0.0200, n = 5$ sham, $n = 6$ MI] (H), the AUC [unpaired two-tailed Student’s *t*-test, $t(9) = 2.917, P = 0.0171, n = 5$ sham, $n = 6$ MI] (I), the peak enhancement [unpaired two-tailed Student’s *t*-test, $t(9) = 4.101, P = 0.0027, n = 5$ sham, $n = 6$ MI] (J) and the correlation between the AUC and the ejection fraction (Pearson’s correlation, $r = -0.3403, R^2 = 0.1158, P = 0.3059, n = 11$) (K). (L) Representative coronal images of parenchymal contrast agent infiltration 20 min after the end of the CM injection, at the level of the hypothalamus (HT) from a sham (top) and a MI (bottom) mouse. Signal enhancement was quantified by parenchymal volumes of interest (VOI, white circles) positioned at the ventral surface of the hypothalamus (HT 1) and 1 mm dorsally (HT 2). Insets highlight the CSF tracer influx at the ventral brain area. (M–P) Characteristics of the CSF tracer influx at the HT 1 VOI, including the time – mean enhancement curve [two-tailed repeated measures two-way ANOVA, Time × Group: $F(25,225) = 2.566, P = 0.0001$; Time: $F(1.786,16.08) = 73.01, P < 0.0001$; Group: $F(1,9) = 9.585, P = 0.0128, n = 5$ sham, $n = 6$ MI] (M), the AUC [unpaired two-tailed Student’s *t*-test, $t(9) = 3.119, P = 0.0123, n = 5$ sham, $n = 6$ MI] (N), the peak enhancement [unpaired two-tailed Student’s *t*-test, $t(9) = 2.449, P = 0.0368, n = 5$ sham, $n = 6$ MI] (O) and the correlation between the AUC and the ejection fraction (Pearson’s correlation, $r = -0.8009, R^2 = 0.6415, P = 0.0031, n = 11$) (P). (Q–T) Characteristics of the CSF tracer influx at the HT 2 VOI, including the time – mean enhancement curve [two-tailed repeated measures two-way ANOVA, Time × Group: $F(25,225) = 3.521, P < 0.0001$; Time: $F(1.699,15.29) = 99.49, P < 0.0001$; Group: $F(1,9) = 5.697, P = 0.0408, n = 5$ sham, $n = 6$ MI] (Q), the AUC [unpaired two-tailed Student’s *t*-test, $t(9) = 2.334, P = 0.0444, n = 5$ sham, $n = 6$ MI] (R), the peak enhancement [unpaired two-tailed Student’s *t*-test, $t(9) = 2.298, P = 0.0471, n = 5$ sham, $n = 6$ MI] (S) and the correlation between the AUC and the ejection fraction (Pearson’s correlation, $r = -0.4749, R^2 = 0.2256, P = 0.1399, n = 11$) (T). Scale bars in C and L = 1 mm; insets = 1 mm. Colour map: C and L = inferno (CSF tracer) overlaid on greyscale (mean anatomical image). Curves are presented as mean ± standard error of the mean (SEM). Level of significance is calculated by two-tailed repeated measures two-way ANOVA with Geisser-Greenhouse correction and represents the *P*-value of the comparison between the Time × Group coefficients, given that there is a significant difference between both the time and group coefficients separately. Box plots represent median, quartiles, min and max values,

(Continued)

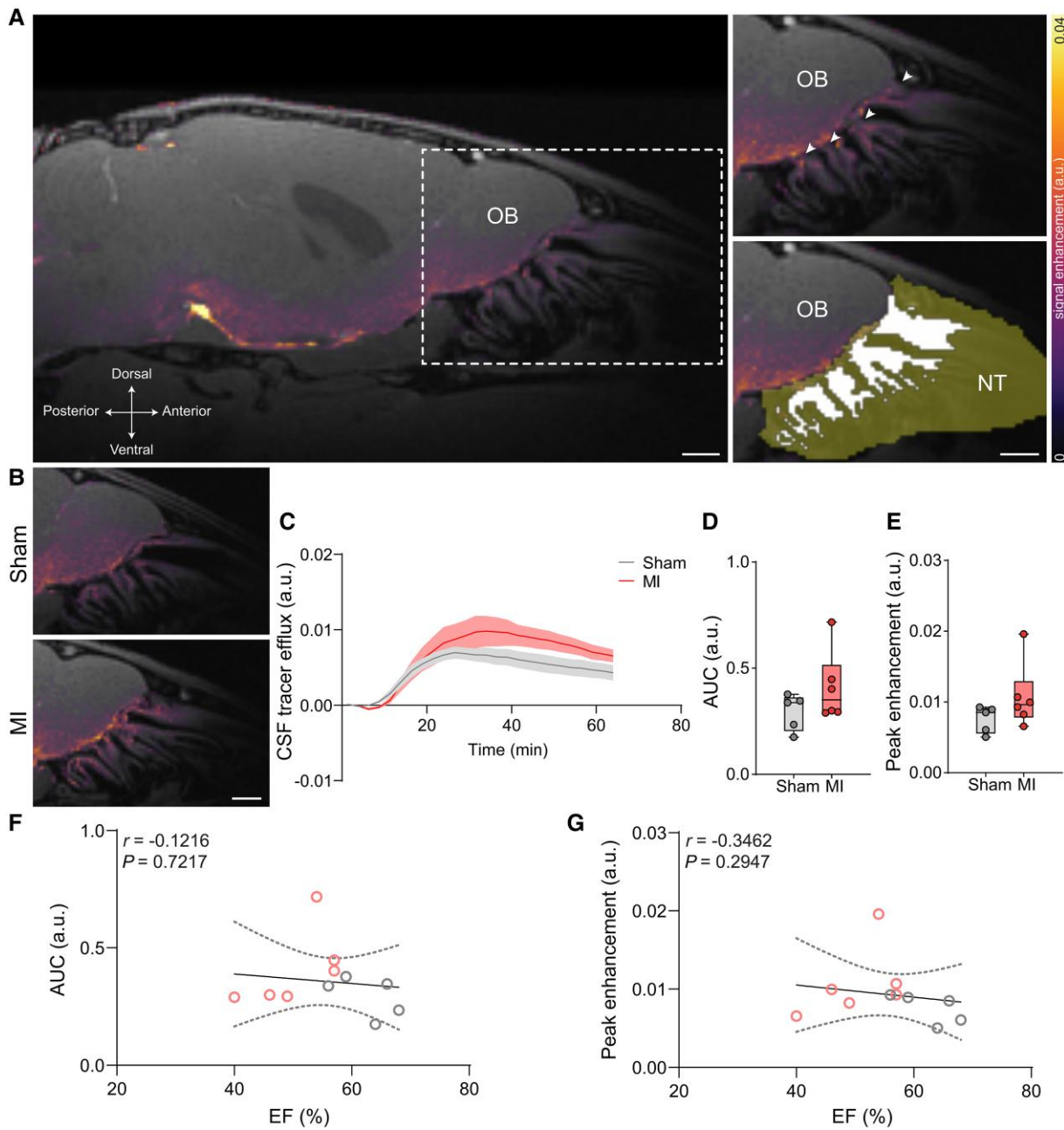


Figure 4 CSF nasal efflux is not affected at 12 weeks post-myocardial infarction. (A) Representative sagittal view of contrast agent distribution 20 min after the end of the cisterna magna (CM) injection (left). Close-up view of the white box, highlighting the olfactory neuron bundles crossing the cribriform plate (top right) and the same area with the nasal turbinates (NT) mask and the significantly enhancing voxels mask overlaid (bottom right). (B) Representative sagittal images of contrast agent distribution 20 min after the end of the CM injection, at the level of the NT from a sham (top) and a myocardial infarction (MI) (bottom) mouse. (C–E) Characteristics of the mean signal enhancement of the significantly enhancing voxels of the nasal turbinates, including the time – mean enhancement curve [two-tailed repeated measures two-way ANOVA, Time \times Group: $F(25,225) = 1.531$, $P = 0.0565$, $n = 5$ sham, $n = 6$ MI] (C), the area under the curve (AUC) (two-tailed Mann-Whitney test, $U = 9$, $P = 0.329$, $n = 5$ sham, $n = 6$ MI) (D) and the peak enhancement (two-tailed Mann-Whitney test, $U = 6$, $P = 0.1255$, $n = 5$ sham, $n = 6$ MI) (E). (F) Correlation between the AUC and the ejection fraction (Pearson’s correlation, $r = -0.1216$, $R^2 = 0.01478$, $P = 0.7217$, $n = 11$). (G) Correlation between the peak enhancement and the ejection fraction (Spearman’s correlation, $r = -0.3462$, $P = 0.2947$, $n = 11$). Scale bars in A and B = 1 mm. Colour map: A and B = inferno (CSF tracer) overlaid on greyscale (mean anatomical image). Curves are presented as mean \pm standard error of the mean (SEM). Box plots represent median, quartiles, min and max values, with individual animals shown as coloured dots. Individual animals are represented as coloured circles in the correlation graphs, red (MI) and grey (sham). EF = ejection fraction; OB = olfactory bulbs.

Figure 3 Continued

with individual animals shown as coloured dots. Individual animals are represented as coloured circles in the correlation graphs, red (MI) and grey (sham). * $P < 0.05$, ** $P < 0.01$, *** $P < 0.001$, **** $P < 0.0001$. 2D-UTE = two-dimensional ultrashort echo time; DCE-MRI = dynamic contrast enhanced-magnetic resonance imaging; K/X = ketamine/xylazine.

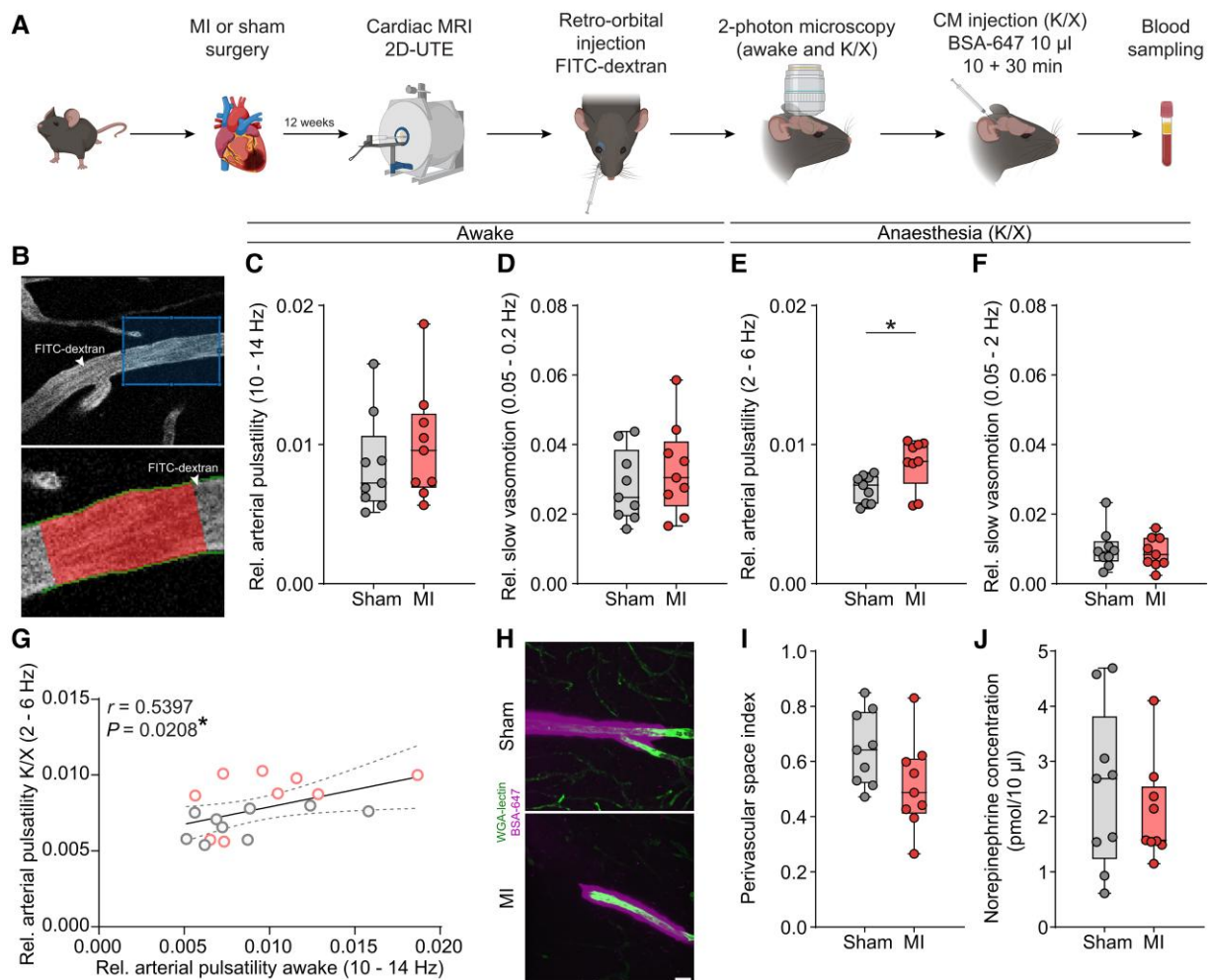


Figure 5 Cerebral arterial pulsatility increases at 12 weeks post-myocardial infarction. (A) Schematic representation of the experimental timeline. (B) *Top*: Representative *in vivo* two-photon fluorescence microscopy image of a pial artery after intravenous injection of FITC-dextran (white arrowheads show vascular segments labelled with FITC-dextran). The blue box indicates the vascular segment used for arterial pulsatility analysis. *Bottom*: The magnified vascular segment from which the vascular diameter oscillations are measured. (C) Arterial pulsatility amplitude, normalized to the vessel diameter, in awake mice (two-tailed Mann-Whitney test, $U = 28$, $P = 0.2973$, $n = 9$ sham, $n = 9$ MI). (D) Slow vasomotion amplitude, normalized to the vessel diameter, in awake mice [unpaired two-tailed Student's *t*-test, $t(16) = 0.8545$, $P = 0.4055$, $n = 9$ sham, $n = 9$ MI]. (E) Arterial pulsatility amplitude, normalized to the vessel diameter, under K/X anaesthesia (two-tailed Mann-Whitney test, $U = 16$, $P = 0.0315$, $n = 9$ sham, $n = 9$ MI). (F) Slow vasomotion amplitude, normalized to the vessel diameter, under K/X anaesthesia [unpaired two-tailed Student's *t*-test, $t(16) = 0.4223$, $P = 0.6784$, $n = 9$ sham, $n = 9$ MI]. (G) Correlation between arterial pulsatility amplitude in awake mice and arterial pulsatility amplitude, under K/X anaesthesia (Spearman's correlation, $r = 0.5397$, $P = 0.0208$, $n = 18$). (H) Representative *ex vivo* images of the perivascular space (visualized with BSA-647) around cerebral vessels (visualized with WGA-488 lectin) from a sham (*top*) and a MI (*bottom*) mouse. (I) Quantification of the perivascular space index. Perivascular space size was calculated by subtracting the lectin signal diameter from the BSA-647 tracer signal diameter. The perivascular space index ratio was then calculated by dividing the tracer signal diameter with the lectin signal diameter. Three diameter measurements across each vessel from four individual vessels were analysed per mouse [unpaired two-tailed Student's *t*-test, $t(16) = 1.873$, $P = 0.0795$, $n = 9$ sham, $n = 9$ MI]. (J) Plasma norepinephrine concentration [unpaired two-tailed Student's *t*-test, $t(16) = 0.7407$, $P = 0.4696$, $n = 9$ sham, $n = 9$ MI]. Scale bar in H = 20 μm . Values in parentheses indicate the frequency range for each measurement. Box plots represent median, quartiles, min and max values, with individual animals shown as coloured dots. Individual animals are represented as coloured circles in the correlation graph, red (MI) and grey (sham). * $P < 0.05$. 2D-UTE = two-dimensional ultrashort echo time; CM = cisterna magna; K/X = ketamine/xylazine; MI = myocardial infarction; WGA = wheat germ agglutinin.

polarization, the polarization index was calculated^{39,40} in different brain regions of MI and sham mice. We found that at 3, 6 and 12 weeks post-surgery (Supplementary Fig. 4A, C and E), AQP4 polarization in hypothalamus, hippocampus and dorsal cortex did not differ between MI and sham (Supplementary Fig. 4B, D and F).

Reportedly, perivascular macrophages regulate CSF flow and glymphatic influx by mediating the degradation of extracellular matrix (ECM) proteins like collagen IV and laminin in the PVS.⁴¹ Collagen IV and laminin coverage were measured in brain sections from mice at different stages of heart failure progression

(Supplementary Fig. 5A, C, E and G) and the deposition of these proteins did not differ between MI and sham mice at any time point tested (Supplementary Fig. 5B, D, F and H). Taken together, these data show that some well documented regulators of glymphatic flow are not affected in this model of HFREF and highlight the complex interplay among several factors that control the glymphatic system.

To test whether blood–brain barrier (BBB) leakage exists in our model at 12 weeks after the infarction, brain sections were stained for IgG.⁴² No evidence of notable IgG staining outside the vessels was observed in the striatum and hypothalamus of both groups at

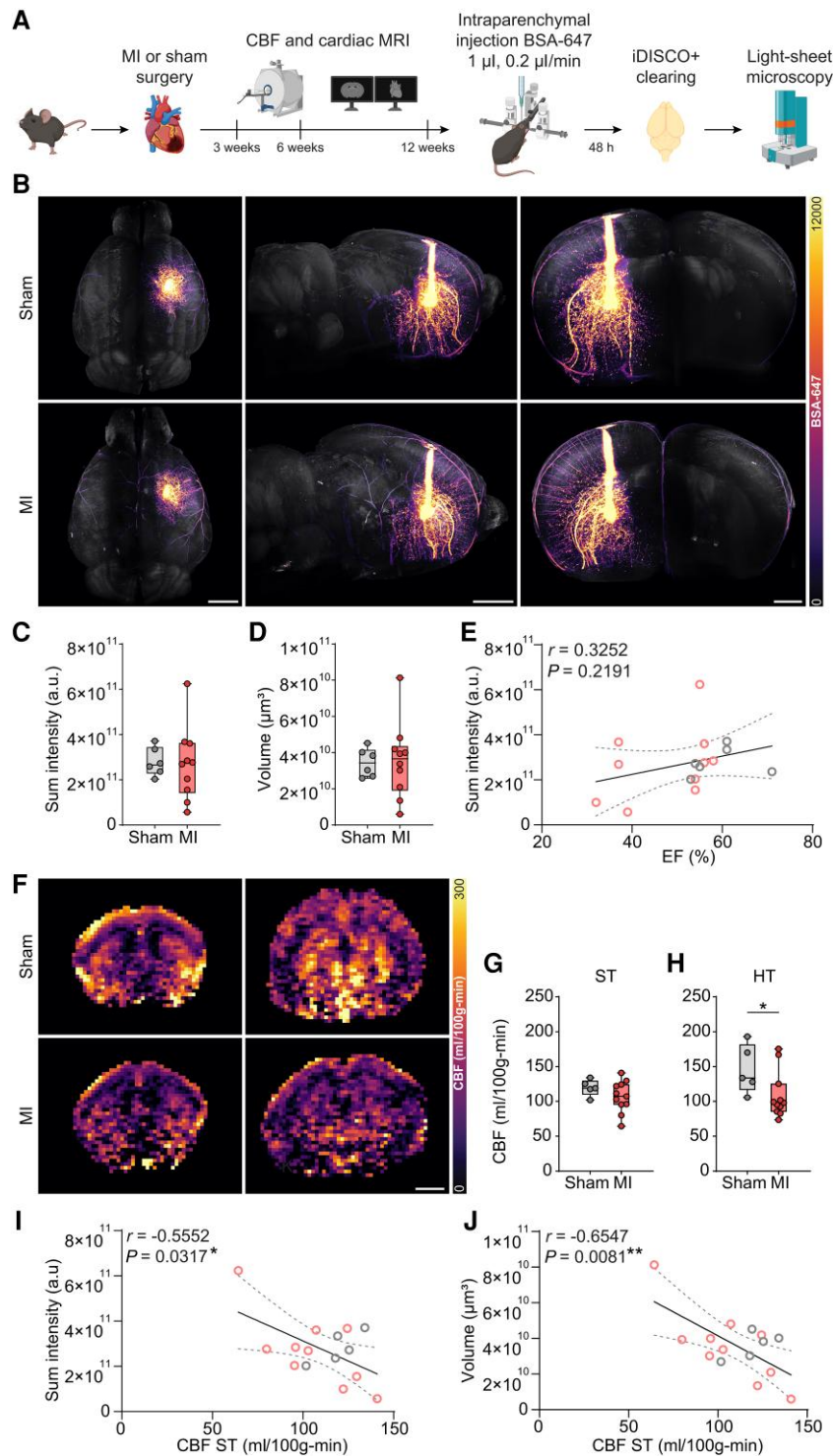


Figure 6 Glymphatic clearance is independent of ejection fraction but decreases with reduced CBF. (A) Schematic representation of the experimental timeline. (B) Representative 3D reconstructed images of optically cleared brains that were isolated 48 h after fluorescent BSA-647 tracer was injected in the striatum of sham (top) and myocardial infarction (MI) (bottom) mice, dorsal view (left), right posterolateral view (middle) and close-up anterior view (right). (C) Quantification of sum fluorescence intensity around the injection site of the tracer [unpaired two-tailed Student's *t*-test, $t(14) = 0.1367$, $P = 0.8932$, $n = 6$ sham, $n = 10$ MI]. (D) Quantification of interstitial tracer volume remaining around the injection site [unpaired two-tailed Student's *t*-test, $t(12.51) = 0.1416$, $P = 0.8897$, $n = 6$ sham, $n = 10$ MI]. (E) Correlation between ejection fraction (EF) and sum fluorescence intensity around the injection site (Pearson's correlation, $r = 0.3252$, $R^2 = 0.1057$, $P = 0.2191$, $n = 16$). (F) Representative cerebral blood flow (CBF) maps acquired using a FAIR-EPI MRI sequence at 12 weeks post-surgery at the level of the striatum (ST, left) and the hypothalamus (HT, right) from sham (top) and MI (bottom) mice. (G) Mean CBF at the ventral striatum at 12 weeks post-MI or sham surgery [unpaired two-tailed Student's *t*-test, $t(14) = 1.191$, $P = 0.2535$, $n = 5$ sham, $n = 11$ MI]. (H) Mean CBF at the hypothalamus at 12 weeks post-MI or sham surgery (two-tailed Mann-Whitney test, $U = 8$, $P = 0.0275$, $n = 5$ sham, $n = 11$ MI). (I) Correlation between mean CBF at the ventral striatum and sum fluorescence intensity around the injection site (Pearson's correlation, $r = -0.5552$, $R^2 = 0.3083$, $P = 0.0317$, $n = 15$). (J) Correlation between mean CBF at the ventral striatum and tracer volume remaining around the

(continued)

this time point where glymphatic influx was increased (Supplementary Fig. 6A). Therefore, BBB leakage is unlikely to have a significant contribution to our results.

Glymphatic clearance is independent of ejection fraction but inversely correlates with cerebral blood flow

Glymphatic clearance of intraparenchymally injected tracers has long been used to indicate adequate glymphatic function, and impaired glymphatic clearance is considered to contribute to cognitive decline.^{22,39} We therefore investigated how glymphatic clearance is affected by HFREF and how it relates to parameters of cardiac function and CBF. For this, cardiac function and CBF in mice subjected to MI or sham surgery were longitudinally monitored using MRI at 3, 6 and 12 weeks post-surgery. Fluorescent BSA-647 tracer was then injected in the striatum of mice at the 12-week time point, and brains were isolated after 48 h (Fig. 6A). The brains were optically cleared and imaged using light-sheet microscopy, comprehensively visualizing the 3D distribution of remaining tracer across the whole brain as a measure of glymphatic clearance (Fig. 6B). Tracer intensity and volume around the injection site did not differ between groups (Fig. 6C and D), and these measures of glymphatic clearance did not significantly correlate with the EF at this time point (Fig. 6E).

For CBF analysis, ventral striatum and hypothalamus were assessed, where increases in glymphatic influx had been found in MI versus sham. No group differences in CBF of either region at 3 (Supplementary Fig. 7A–C) or 6 weeks post-surgery (Supplementary Fig. 7D–F) were found. However, our analysis at 12 weeks identified a statistically significant decrease in the hypothalamus of MI mice, while CBF at the striatum did not differ between the groups (Fig. 6F–H). Intriguingly, it was found that tracer intensity and volume after intraparenchymal injection in the striatum had a significant inverse correlation with CBF at this area (Fig. 6I and J). These findings suggest that unlike glymphatic influx, clearance is neither dependent on EF nor affected by HFREF at the same time points. They also revealed a previously unknown connection between glymphatic clearance and CBF.

HFREF leads to proportionately larger brain parenchyma and smaller cerebral ventricles at 12 weeks post-MI

At 12 weeks post-MI, we found that glymphatic influx and clearance did not exhibit similar dynamics. This prompted us to analyse the structural MRI scans to evaluate brain volume in mice at this time point (Fig. 7A). Our analysis revealed that while whole brain volumes remained comparable between MI and sham groups (Fig. 7B), there was a significant reduction in cerebral ventricular volume in MI mice (Fig. 7C). Notably, this decrease in ventricular volume persisted even after normalizing for whole brain volume (Fig. 7D). Correspondingly, the brain parenchyma of MI mice showed a proportional increase compared to the sham group

(Fig. 7E). These findings suggest that HFREF leads to changes in the brain that are consistent with fluid stagnation in the brain. This abnormality could explain the increased CSF influx to the brain via perivascular pathways in heart failure, and why this was not associated with more solute clearance from the brain.

Discussion

Here, a multimodal approach was used to investigate the impact of HFREF on the glymphatic system of the brain. For this purpose, a mouse model of heart failure was used, induced by MI, causing dilation of the LV and impaired systolic function.⁴³ Previous work using this model has shown that cognitive impairment occurs as heart failure progresses.^{25,44,45} Clinical studies have also associated low EF with cognitive decline and CSF biomarkers of Alzheimer's disease.^{46–48}

Glymphatic dysfunction has been established as a major mechanism contributing to cognitive impairment and dementia,²² with impaired glymphatic function resulting in increased amyloid- β burden in the brain.^{39,49,50} Type II diabetes mellitus is a disease which is characterized by increased glymphatic influx and impaired glymphatic clearance, and interestingly this mismatch correlates with the degree of cognitive decline.^{51,52} Our findings reveal a progressive dysregulation of glymphatic system homeostasis in HFREF, leading to a similar case of mismatch between glymphatic influx and clearance. While structural and functional changes in the heart were already observed at 3 weeks post-MI, glymphatic influx was not affected and did not correlate with EF at that time point. Surprisingly, at 6 and 12 weeks post-MI, an increase in glymphatic influx proportionate to the reduction in EF was found. Despite the increase in influx, glymphatic clearance was not proportionately affected at 12 weeks post-MI, indicating a dysregulation of the system. This was highlighted by an increase in relative brain parenchymal volume in MI mice, which could indicate stagnation of brain fluid. Whether this fluid is intra- or extracellular, and whether it could be the source of further brain pathology in heart failure, have yet to be investigated.

Glymphatic influx is dependent on tracer size, as evidenced by fluoroscopy and MRI studies.^{9,53} We found that increased glymphatic influx occurs at 12 weeks post-MI, when using both GBCA with small molecular weight (Dotarem[®], 753.9 Da) and a much larger fluorescent tracer (BSA-647, 66 kDa). Of note, the EF inversely correlated with glymphatic influx in both experiments, thus highlighting the efficacy of both methodologies and their complementary nature in studying the glymphatic system.

Several factors have been reported to regulate glymphatic influx and clearance. Loss of perivascular AQP4 polarization leads to impaired glymphatic function and has been reported in healthy ageing and in several disease models,^{39,54–56} while enhanced AQP4 polarization was associated with increased glymphatic influx in the hypothalamus of mice fed with a high-fat diet.³⁰ However, our analysis did not show differences in AQP4 polarization at any time point after MI.

Figure 6 (Continued)

injection site (Pearson's correlation, $r = -0.6547$, $R^2 = 0.4287$, $P = 0.0081$, $n = 15$). Scale bars in B, left = 2 mm, middle = 2 mm, right = 1 mm; F = 2 mm. Colour map: B = inferno (BSA-647) overlaid on greyscale (anatomical reference); F = inferno. Box plots represent median, quartiles, min and max values, with individual animals shown as coloured dots. Individual animals are represented as coloured circles in the correlation graphs, red (MI) and grey (sham). * $P < 0.05$, ** $P < 0.01$. FAIR-EPI = Flow-sensitive Alternating Inversion Recovery Echo-Planar Imaging; iDISCO = immunolabelling-enabled 3D imaging of solvent-cleared organs.

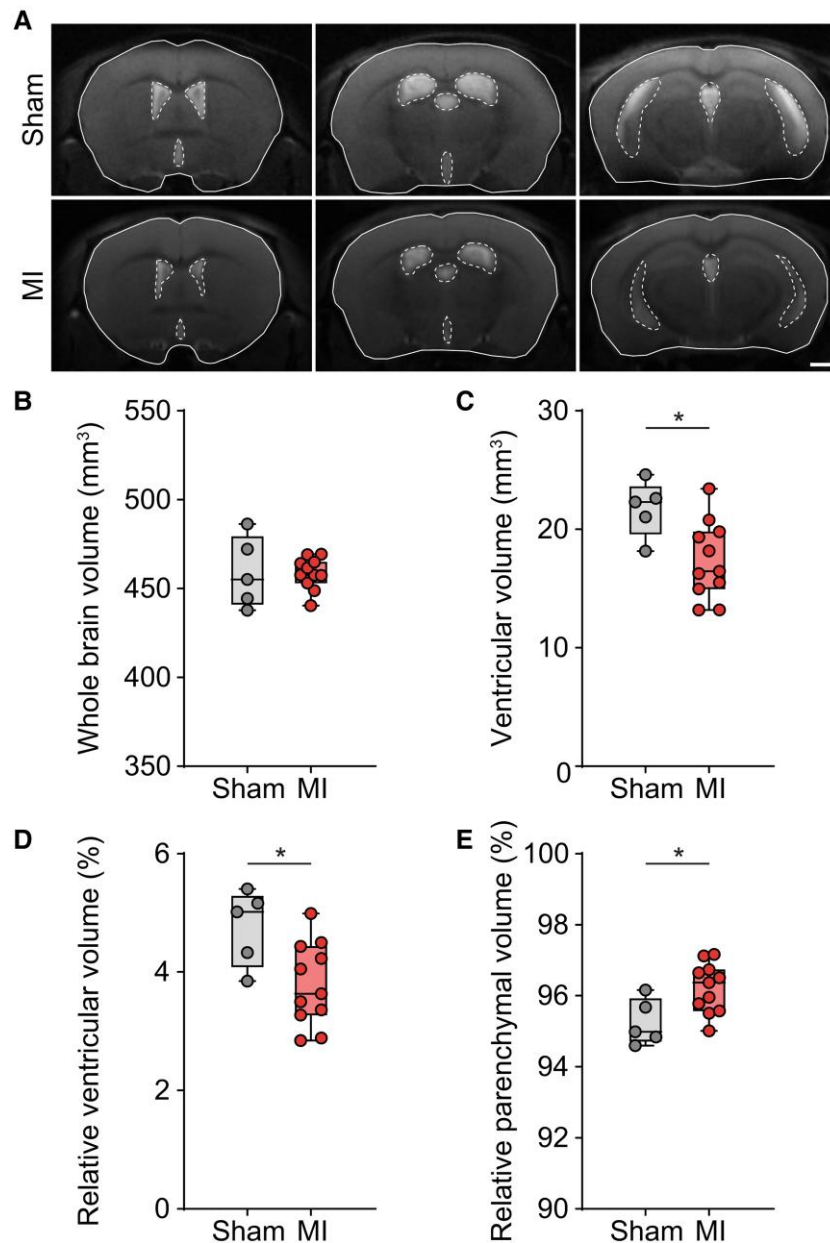


Figure 7 Proportionately larger brain parenchyma and smaller cerebral ventricles at 12 weeks post-myocardial infarction. (A) Representative coronal brain images acquired using a RARE sequence at 12 weeks post-surgery at three levels along the anteroposterior axis from a sham (top) and a myocardial infarction (MI) (bottom) mouse (brain masks marked with white lines and ventricular masks marked with white dashed lines). (B) Whole brain volume at 12 weeks post-MI or sham surgery [unpaired two-tailed Welch's t-test, $t(4.712) = 0.06554$, $P = 0.9504$, $n = 5$ sham, $n = 11$ MI]. (C) Ventricular volume at 12 weeks post-MI or sham surgery [unpaired two-tailed Student's t-test, $t(14) = 2.685$, $P = 0.0178$, $n = 5$ sham, $n = 11$ MI]. (D) Relative ventricular volume at 12 weeks post-MI or sham surgery [unpaired two-tailed Student's t-test, $t(14) = 2.608$, $P = 0.0207$, $n = 5$ sham, $n = 11$ MI]. (E) Relative brain parenchymal volume at 12 weeks post-MI or sham surgery [unpaired two-tailed Student's t-test, $t(14) = 2.608$, $P = 0.0207$, $n = 5$ sham, $n = 11$ MI]. Scale bar in A = 1 mm. Box plots represent median, quartiles, min and max values, with individual animals shown as coloured dots. RARE = rapid acquisition with refocused echoes.

A recent study reported that LYVE1⁺ perivascular macrophages regulate ECM remodelling in the PVS and thereby arterial motion and CSF flow. This study also identified these cells as important regulators of CSF flow dynamics in ageing and Alzheimer's disease.⁴¹ Our analysis of ECM proteins, such as collagen IV and laminin in brain sections of MI and sham mice, did not reveal significant differences at any time point.

A study using the coronary artery ligation model in rats reported BBB leakage compared to sham rats 4 weeks after the surgery.⁵⁷ However, evidence of BBB leakage was not found at our 12-week

time point. While it has been hypothesized that BBB disruption could be harmful to perivascular flow,^{32,58} the effect of BBB leakage to the glymphatic system has not yet been tested experimentally and remains to be investigated as we did not observe BBB deficits in our model.

Using two-photon microscopy, the arterial pulsatility of pial arteries was measured and was found to be increased in mice at 12 weeks post-MI relative to sham. Arterial pulsatility is a well documented driver of glymphatic influx^{18,19} and its increase provides a plausible mechanism for the observed increase in glymphatic

influx. Interestingly, this effect in arterial pulsatility was only evident under K/X anaesthesia and not in awake mice, emphasizing the importance of sleep and anaesthesia in glymphatic function.⁵⁹ On the other hand, slow vasomotion (centred around ~0.1 Hz), which is caused by oscillations in neuronal activity and smooth muscle cell contractility and occurs independently of pulsatile blood flow,⁶⁰ was not affected by heart failure. While evoked vascular reactivity (functional hyperaemia) has been shown to increase both glymphatic influx and clearance,^{35,61} our baseline measurement of slow vasomotion did not differ between MI and sham mice both in the awake state and under K/X anaesthesia. Whether this increase in cerebral arterial pulsatility is a consequence of heart failure or a compensatory mechanism of the brain trying to preserve glymphatic homeostasis remains to be elucidated.

To address whether increased glymphatic influx was influenced by downstream impairment of CSF efflux, DCE-MRI was used to measure the movement of injected GBCA through the cribriform plate, a major CSF efflux route.^{14,33,34} Although our analysis did not reveal significant differences in nasal CSF efflux, the potential contribution of other CSF efflux pathways was not accounted for. Meningeal lymphatics constitute another pathway for the clearance of CSF and macromolecules.^{62,63} However, the relative contribution of each of these pathways to CSF efflux remains to be determined.¹⁴ We also used confocal microscopy to assess the relative width of the PVS. A mouse study on ocular glymphatic transport in type I diabetes found that repeated transient hyperglycaemia induced an increase in ocular glymphatic transport, by a mechanism involving PVS enlargement.⁶⁴ Our analysis found no such differences in PVS size between MI and sham at 12 weeks post-surgery. The increased glymphatic influx observed is therefore unlikely attributable to reduced CSF efflux to the periphery or CSF pooling in the PVS. Application of continuous positive airway pressure reportedly increases CSF flow speed and glymphatic transport via intracranial pressure (ICP) increases.⁶⁵ As ICP was not measured in this study, it cannot be excluded that potential ICP differences between our groups influenced the observed increase in glymphatic influx. Similarly, blood pressure has an established influence on the glymphatic system^{20,66} and was not measured in this study. Previous work with this model of HFrEF has reported that mean arterial pressure decreases in MI mice compared to sham from 2 weeks post-MI⁶⁷ and remains reduced at 6 and 12 weeks post-MI,^{45,67–69} thereby eliminating a potential confounder from our study.

Reduced CBF has been identified as an early sign of several neurodegenerative diseases⁷⁰ and is commonly found in patients with heart failure.⁷¹ While cerebral autoregulation can normally compensate for reductions in cardiac output by lowering cerebrovascular resistance, this is not the case in heart failure, where cerebrovascular reactivity is compromised.^{72,73} Instead, cerebral arteries display a TNF α -dependent increase in myogenic tone, resulting in elevated cerebrovascular resistance and therefore reduced CBF.⁶⁷ In this study, a reduction in CBF was found in the hypothalamus of mice at 12 weeks post-MI, while CBF in the striatum was not significantly affected. Previous studies with this mouse model of HFrEF have reported a decrease in CBF at the dorsal cortex⁴⁵ but lack of perfusion deficits at the hippocampus at 12-weeks post-MI,²⁵ indicating that cerebrovascular reactivity is not uniformly compromised. Intriguingly, our analysis found an association between CBF at the striatum and glymphatic clearance from that region. As progressive HFrEF eventually results in CBF reduction, it can be expected that glymphatic clearance

further deteriorates, leading to neurodegeneration. Therefore, this study paves the way for further research on the connection between CBF and the glymphatic system. This connection needs to be investigated and validated in other disease models where CBF is compromised to determine if it can be consistently used as an indicator of glymphatic clearance. This result should also be interpreted in the context of other factors affecting glymphatic clearance. For example, isoflurane is an anaesthetic that exerts a vasodilatory effect on cerebral vessels,⁷⁴ increasing CBF, while at the same time it has been shown to inhibit glymphatic function.^{31,75,76} However, isoflurane strongly reduced arterial vasomotion, an important driving force for glymphatic clearance,³⁵ while it was also correlated with lower delta power, which is important for glymphatic function.⁷⁵ Over the years, it has become evident that glymphatic clearance relies on a delicate balance among several fine-tuned factors. Changes to each of these parameters exert a partial effect on clearance, however, it is the combined effect of all these together that results in the observed outcome after a drug administration or a disease condition. This study suggests that CBF might be yet another parameter affecting glymphatic clearance.

There is a well-established relationship between neurodegeneration and heart failure in both patients and animal models.^{8,25,44,77,78} Recent findings have pinpointed neurons as key regulators of glymphatic flow. Imaging studies in humans have revealed that neuronal activity is linked to haemodynamics and CSF oscillations during sleep.⁷⁹ Studies in mice have shown that neuronal activity correlates with glymphatic function⁵⁹ under different brain states and anaesthetic regimens.⁷⁵ Furthermore, during sleep or ketamine anaesthesia, neurons were reported to generate large-amplitude ionic oscillations in the ISF that facilitate glymphatic flow,⁸⁰ while multisensory 40 Hz (gamma) stimulation promoted glymphatic clearance in the cerebral cortex of mice.⁸¹ Therefore, as neurodegeneration worsens during heart failure progression, it is postulated that the ability of neurons to regulate their waste clearance progressively declines.

The hormone and neurotransmitter norepinephrine has an important role in regulating glymphatic activity.⁵⁹ Increased CSF-ISF exchange during sleep is attributed to lower locus coeruleus-derived noradrenergic tone inducing an increased interstitial space volume fraction.^{59,82} Therefore, in the transition from wakefulness to sleep, as central norepinephrine levels decline, expansion of the extracellular space results in decreased tissue resistance and leads to faster glymphatic influx and clearance.⁵⁹ Although plasma norepinephrine levels did not significantly differ between MI and sham in our study, they are part of the compensatory homeostatic responses that occur in HFrEF⁸³ and are important predictors of mortality and morbidity.^{84,85} The interplay between brain and plasma norepinephrine levels during heart failure progression and their effect on the glymphatic system need to be investigated further.

Only male mice were used in this study. Female sex has been reported to be protective following permanent LAD ligation, with female mice showing improved recovery and heart function following MI.⁸⁶ The aim of this study was to investigate the effects of a severe HFrEF phenotype and male mice develop greater hypertrophy, more prominent LV dilation and LV dysfunction in this model of HFrEF.⁸⁷ However, given that glymphatic influx is not affected by sex,⁸⁸ future studies should investigate whether the association between EF and glymphatic influx is consistent between the sexes.

Although the LAD ligation model is the most commonly used model of MI leading to HFrEF, it does not fully reflect the

development of heart failure in patients. Many factors causing MI in humans, including coronary artery disease, atherosclerosis and hypertension, are not present in this model.⁸⁹ However, this allowed us to study—in isolation—the effects of systolic dysfunction and reduced EF absent other confounds. Further investigation of the interaction between the glymphatic system and heart failure in the presence of comorbidities is warranted. The study focused on 12 weeks post-MI as cardiac injury is considered stable at this time point, therefore resembling a more chronic disease stage.^{45,89} Further studies should investigate how the glymphatic system is affected at earlier time points to potentially identify the optimal time for an intervention before the onset of glymphatic dysfunction.

Similarly, future studies should investigate the effects of different models of heart failure, including heart failure with preserved ejection fraction (HFpEF), on the glymphatic system. HFpEF cases account for ~50% of patients with heart failure and there is a strong association with various comorbidities including hypertension, obesity and diabetes mellitus.^{90,91} Therefore, it would be valuable to study how different mechanisms of cardiac dysfunction affect the glymphatic system when the EF is not compromised.

Data availability

The data that support the findings of this study are available from the corresponding author, upon reasonable request. CBF fit code and group statistical analyses are openly available online at <https://doi.org/10.5281/zenodo.11475856>.⁹²

Acknowledgements

We thank Dr Gustav Strijkers, Amsterdam UMC, Amsterdam for allowing us to incorporate the binning routines of the cardiac radial data from Retrospective 8.1 (github <https://github.com/Moby1971>) into our own scripts for image reconstruction. Lund University Bioimaging Centre (LBIC), Lund University, is gratefully acknowledged for providing experimental resources. Schematic illustrations were created with BioRender.com. Kritsilis, M. (2024) <https://biorender.com/p84s069> (Fig. 1); <https://biorender.com/d51g032> (Fig. 2); <https://biorender.com/d34n984> (Fig. 3); <https://biorender.com/k34m050> (Fig. 5); <https://biorender.com/x19q973> (Fig. 6); <https://biorender.com/t91i158> (Supplementary Fig. 2); <https://biorender.com/r16a393> (Supplementary Fig. 3). The thumbnail image for the online table of contents was created in BioRender. Kritsilis, M. (2024) <https://biorender.com/v46z271>.

Funding

This work was supported by the Swedish Research Council VR (2022-02727) (I.L.), the Olle Engkvist Foundation (208-0622, 204-0279) (I.L.), the Knut and Alice Wallenberg foundation (F 2015/2112) (I.L. and A.M.), The Swedish Foundation for International Cooperation in Research and Higher Education-STINT (MG19-8469) and the University of Augsburg (A.M.), the Wenner-Gren Stiftelserna (UPD2019-0049 and UPD2020-0129) (I.L.) and the Endowments for the Natural Sciences, Medicine and Technology—Medicine (Royal Physiographic Society of Lund) (N.S.), the Lundbeck foundation (R359-2021-165 and R347-2020-1659), the Dr. Miriam and Sheldon G. Adelson Medical Research Foundation, the Novo Nordisk Foundation Laureate Continuation Grant

(NNF20OC0066419) (M.N.), and the National Institutes of Health—NIH grant U19NS128613 (K.B.).

Competing interests

The authors report no competing interests.

Supplementary material

Supplementary material is available at *Brain* online.

References

1. Groenewegen A, Rutten FH, Mosterd A, Hoes AW. Epidemiology of heart failure. *Eur J Heart Fail.* 2020;22:1342-1356.
2. Wu Y, Chen L, Zhong F, et al. Cognitive impairment in patients with heart failure: Molecular mechanism and therapy. *Heart Fail Rev.* 2023;28:807-820.
3. Qiu C, Winblad B, Marengoni A, Klarin I, Fastbom J, Fratiglioni L. Heart failure and risk of dementia and Alzheimer disease: A population-based cohort study. *Arch Intern Med.* 2006;166:1003-1008.
4. Vogels RL, Scheltens P, Schroeder-Tanka JM, Weinstein HC. Cognitive impairment in heart failure: A systematic review of the literature. *Eur J Heart Fail.* 2007;9:440-449.
5. Cannon JA, Moffitt P, Perez-Moreno AC, et al. Cognitive impairment and heart failure: Systematic review and meta-analysis. *J Card Fail.* 2017;23:464-475.
6. Cermakova P, Eriksdotter M, Lund LH, Winblad B, Religa P, Religa D. Heart failure and Alzheimer's disease. *J Intern Med.* 2015;277:406-425.
7. Maroofi A, Moro T, Agrimi J, Safari F. Cognitive decline in heart failure: Biomolecular mechanisms and benefits of exercise. *Biochim Biophys Acta Mol Basis Dis.* 2022;1868:166511.
8. Alosco ML, Hayes SM. Structural brain alterations in heart failure: A review of the literature and implications for risk of Alzheimer's disease. *Heart Fail Rev.* 2015;20:561-571.
9. Iliff JJ, Wang M, Liao Y, et al. A paravascular pathway facilitates CSF flow through the brain parenchyma and the clearance of interstitial solutes, including amyloid β . *Sci Transl Med.* 2012;4:147ra111.
10. Mestre H, Hablitz LM, Xavier AL, et al. Aquaporin-4-dependent glymphatic solute transport in the rodent brain. *Elife.* 2018;7:e40070.
11. Gomolka RS, Hablitz LM, Mestre H, et al. Loss of aquaporin-4 results in glymphatic system dysfunction via brain-wide interstitial fluid stagnation. *Elife.* 2023;12:e82232.
12. Aspelund A, Antila S, Proulx ST, et al. A dural lymphatic vascular system that drains brain interstitial fluid and macromolecules. *J Exp Med.* 2015;212:991-999.
13. Louveau A, Smirnov I, Keyes TJ, et al. Structural and functional features of central nervous system lymphatic vessels. *Nature.* 2015;523:337-341.
14. Proulx ST. Cerebrospinal fluid outflow: A review of the historical and contemporary evidence for arachnoid villi, perineural routes, and dural lymphatics. *Cell Mol Life Sci.* 2021;78:2429-2457.
15. Shah T, Leurgans SE, Mehta RI, et al. Arachnoid granulations are lymphatic conduits that communicate with bone marrow and dura-arachnoid stroma. *J Exp Med.* 2023;220:e20220618.
16. Smyth LCD, Xu D, Okar SV, et al. Identification of direct connections between the dura and the brain. *Nature.* 2024;627:165-173.

17. Ringstad G, Eide PK. Cerebrospinal fluid tracer efflux to parasagittal dura in humans. *Nat Commun.* 2020;11:354.
18. Iliff JJ, Wang M, Zeppenfeld DM, et al. Cerebral arterial pulsation drives paravascular CSF–interstitial fluid exchange in the murine brain. *J Neurosci.* 2013;33:18190–18199.
19. Mestre H, Tithof J, Du T, et al. Flow of cerebrospinal fluid is driven by arterial pulsations and is reduced in hypertension. *Nat Commun.* 2018;9:4878.
20. Mortensen KN, Sanggaard S, Mestre H, et al. Impaired glymphatic transport in spontaneously hypertensive rats. *J Neurosci.* 2019;39:6365–6377.
21. Romay MC, Knutsen RH, Ma F, et al. Age-related loss of Notch3 underlies brain vascular contractility deficiencies, glymphatic dysfunction, and neurodegeneration in mice. *J Clin Invest.* 2024;134:e166134.
22. Nedergaard M, Goldman SA. Glymphatic failure as a final common pathway to dementia. *Science.* 2020;370:50–56.
23. Xu Z, Xiao N, Chen Y, et al. Deletion of aquaporin-4 in APP/PS1 mice exacerbates brain A β accumulation and memory deficits. *Mol Neurodegener.* 2015;10:58.
24. Wurm R, Prausmüller S, Ponleitner M, et al. Serum markers of neurodegeneration are strongly linked to heart failure severity and outcome. *JACC Heart Fail.* 2024;12:1073–1085.
25. Vanherle L, Lidington D, Uhl FE, et al. Restoring myocardial infarction-induced long-term memory impairment by targeting the cystic fibrosis transmembrane regulator. *EBioMedicine.* 2022;86:104384.
26. In 't Zandt R, Mahmutovic Persson I, Tibiletti M, von Wachenfeldt K, Parker GJM, Olsson LE. Contrast enhanced longitudinal changes observed in an experimental bleomycin-induced lung fibrosis rat model by radial DCE-MRI at 9.4T. *PLoS One.* 2024;19:e0310643.
27. Xavier ALR, Hauglund NL, von Holstein-Rathlou S, et al. Cannula implantation into the cisterna magna of rodents. *J Vis Exp.* 2018;135:57378.
28. Schindelin J, Arganda-Carreras I, Frise E, et al. Fiji: An open-source platform for biological-image analysis. *Nat Methods.* 2012;9:676–682.
29. Renier N, Wu Z, Simon DJ, Yang J, Ariel P, Tessier-Lavigne M. iDISCO: A simple, rapid method to immunolabel large tissue samples for volume imaging. *Cell.* 2014;159:896–910.
30. Delle C, Cankar N, Digebjerg Holgersson C, et al. Long-term high-fat diet increases glymphatic activity in the hypothalamus in mice. *Sci Rep.* 2023;13:4137.
31. Stanton EH, Persson NDÁ, Gomolka RS, et al. Mapping of CSF transport using high spatiotemporal resolution dynamic contrast-enhanced MRI in mice: Effect of anesthesia. *Magn Reson Med.* 2021;85:3326–3342.
32. Rasmussen MK, Mestre H, Nedergaard M. Fluid transport in the brain. *Physiol Rev.* 2022;102:1025–1151.
33. Johnston M, Zakharov A, Papaiconomou C, Salmasi G, Armstrong D. Evidence of connections between cerebrospinal fluid and nasal lymphatic vessels in humans, non-human primates and other mammalian species. *Cerebrospinal Fluid Res.* 2004;1:2.
34. Spera I, Cousin N, Ries M, et al. Open pathways for cerebrospinal fluid outflow at the cribriform plate along the olfactory nerves. *EBioMedicine.* 2023;91:104558.
35. van Veluw SJ, Hou SS, Calvo-Rodriguez M, et al. Vasomotion as a driving force for paravascular clearance in the awake mouse brain. *Neuron.* 2020;105:549–561.e5.
36. Kiviniemi V, Wang X, Korhonen V, et al. Ultra-fast magnetic resonance encephalography of physiological brain activity—Glymphatic pulsation mechanisms? *J Cereb Blood Flow Metab.* 2016;36:1033–1045.
37. Wang X, Delle C, Peng W, et al. Age- and glaucoma-induced changes to the ocular glymphatic system. *Neurobiol Dis.* 2023;188:106322.
38. Bojarskaite L, Nafari S, Ravnanger AK, et al. Role of aquaporin-4 polarization in extracellular solute clearance. *Fluids Barriers CNS.* 2024;21:28.
39. Kress BT, Iliff JJ, Xia M, et al. Impairment of paravascular clearance pathways in the aging brain. *Ann Neurol.* 2014;76:845–861.
40. Pavan C, LR Xavier A, Ramos M, et al. DNase treatment prevents cerebrospinal fluid block in early experimental pneumococcal meningitis. *Ann Neurol.* 2021;90:653–669.
41. Drieu A, Du S, Storck SE, et al. Parenchymal border macrophages regulate the flow dynamics of the cerebrospinal fluid. *Nature.* 2022;611:585–593.
42. Lau K, Porschen LT, Richter F, Gericke B. Microvascular blood-brain barrier alterations in isolated brain capillaries of mice over-expressing alpha-synuclein (Thy1-aSyn line 61). *Neurobiol Dis.* 2023;187:106298.
43. Ertl G, Frantz S. Healing after myocardial infarction. *Cardiovasc Res.* 2005;66:22–32.
44. Meissner A, Visanji NP, Momen MA, et al. Tumor necrosis factor- α underlies loss of cortical dendritic spine density in a mouse model of congestive heart failure. *J Am Heart Assoc.* 2015;4:e001920.
45. Lidington D, Fares JC, Uhl FE, et al. CFTR therapeutics normalize cerebral perfusion deficits in mouse models of heart failure and subarachnoid hemorrhage. *JACC Basic Transl Sci.* 2019;4:940–958.
46. Kresge HA, Liu D, Gupta DK, et al. Lower left ventricular ejection fraction relates to cerebrospinal fluid biomarker evidence of neurodegeneration in older adults. *J Alzheimers Dis.* 2020;74:965–974.
47. Jefferson AL, Himali JJ, Au R, et al. Relation of left ventricular ejection fraction to cognitive aging (from the Framingham Heart Study). *Am J Cardiol.* 2011;108:1346–1351.
48. Zheng YM, Zhao YY, Zhang T, et al. Left ventricular ejection fraction and cerebrospinal fluid biomarkers of Alzheimer's disease pathology in cognitively normal older adults: The CABLE study. *J Alzheimers Dis.* 2021;81:743–750.
49. Peng W, Acharyar TM, Li B, et al. Suppression of glymphatic fluid transport in a mouse model of Alzheimer's disease. *Neurobiol Dis.* 2016;93:215–225.
50. Shokri-Kojori E, Wang GJ, Wiers CE, et al. β -amyloid accumulation in the human brain after one night of sleep deprivation. *Proc Natl Acad Sci U S A.* 2018;115:4483–4488.
51. Jiang Q, Zhang L, Ding G, et al. Impairment of the glymphatic system after diabetes. *J Cereb Blood Flow Metab.* 2017;37:1326–1337.
52. Boyd ED, Zhang L, Ding G, et al. The glymphatic response to the development of type 2 diabetes. *Biomedicines.* 2024;12:401.
53. Iliff JJ, Lee H, Yu M, et al. Brain-wide pathway for waste clearance captured by contrast-enhanced MRI. *J Clin Invest.* 2013;123:1299–1309.
54. Iliff JJ, Chen MJ, Plog BA, et al. Impairment of glymphatic pathway function promotes tau pathology after traumatic brain injury. *J Neurosci.* 2014;34:16180–16193.
55. Harrison IF, Ismail O, Machhada A, et al. Impaired glymphatic function and clearance of tau in an Alzheimer's disease model. *Brain.* 2020;143:2576–2593.
56. Ishida K, Yamada K, Nishiyama R, et al. Glymphatic system clears extracellular tau and protects from tau aggregation and neurodegeneration. *J Exp Med.* 2022;219:e20211275.
57. Yu Y, Weiss RM, Wei SG. Interleukin 17A contributes to blood-brain barrier disruption of hypothalamic paraventricular nucleus in rats with myocardial infarction. *J Am Heart Assoc.* 2024;13:e032533.

58. Verheggen ICM, Van Boxtel MPJ, Verhey FRJ, Jansen JFA, Backes WH. Interaction between blood-brain barrier and glymphatic system in solute clearance. *Neurosci Biobehav Rev.* 2018;90:26-33.
59. Xie L, Kang H, Xu Q, et al. Sleep drives metabolite clearance from the adult brain. *Science.* 2013;342:373-377.
60. Mateo C, Knutsen PM, Tsai PS, Shih AY, Kleinfeld D. Entrainment of arteriole vasomotor fluctuations by neural activity is a basis of blood-oxygenation-level-dependent “resting-state” connectivity. *Neuron.* 2017;96:936-948.e3.
61. Holstein-Rønsbo S, Gan Y, Giannetto MJ, et al. Glymphatic influx and clearance are accelerated by neurovascular coupling. *Nat Neurosci.* 2023;26:1042-1053.
62. Ahn JH, Cho H, Kim JH, et al. Meningeal lymphatic vessels at the skull base drain cerebrospinal fluid. *Nature.* 2019;572:62-66.
63. Da Mesquita S, Louveau A, Vaccari A, et al. Functional aspects of meningeal lymphatics in ageing and Alzheimer’s disease. *Nature.* 2018;560:185-191.
64. Delle C, Wang X, Giannetto M, et al. Transient but not chronic hyperglycemia accelerates ocular glymphatic transport. *Fluids Barriers CNS.* 2024;21:26.
65. Ozturk B, Koundal S, Al Bizri E, et al. Continuous positive airway pressure increases CSF flow and glymphatic transport. *JCI Insight.* 2023;8:e170270.
66. Jukkola J, Kaakinen M, Singh A, et al. Blood pressure lowering enhances cerebrospinal fluid efflux to the systemic circulation primarily via the lymphatic vasculature. *Fluids Barriers CNS.* 2024;21:12.
67. Yang J, Hossein Noyan-Ashraf M, Meissner A, et al. Proximal cerebral arteries develop myogenic responsiveness in heart failure via tumor necrosis factor- α -dependent activation of sphingosine-1-phosphate signaling. *Circulation.* 2012;126:196-206.
68. Hoefler J, Azam MA, Kroetsch JTE, et al. Sphingosine-1-phosphate-dependent activation of p38 MAPK maintains elevated peripheral resistance in heart failure through increased myogenic vasoconstriction. *Circ Res.* 2010;107:923-933.
69. Meissner A, Yang J, Kroetsch JT, et al. Tumor necrosis factor- α -mediated downregulation of the cystic fibrosis transmembrane conductance regulator drives pathological sphingosine-1-phosphate signaling in a mouse model of heart failure. *Circulation.* 2012;125:2739-2750.
70. Iadecola C. The neurovascular unit coming of age: A journey through neurovascular coupling in health and disease. *Neuron.* 2017;96:17-42.
71. Roy B, Woo MA, Wang DJJ, Fonarow GC, Harper RM, Kumar R. Reduced regional cerebral blood flow in patients with heart failure. *Eur J Heart Fail.* 2017;19:1294-1302.
72. Georgiadis D. Cerebrovascular reactivity is impaired in patients with cardiac failure. *Eur Heart J.* 2000;21:407-413.
73. Choi BR, Kim JS, Yang YJ, et al. Factors associated with decreased cerebral blood flow in congestive heart failure secondary to idiopathic dilated cardiomyopathy. *Am J Cardiol.* 2006;97:1365-1369.
74. Munting LP, Derieppe MPP, Suidgeest E, Denis de Senneville B, Wells JA, van der Weerd L. Influence of different isoflurane anesthesia protocols on murine cerebral hemodynamics measured with pseudo-continuous arterial spin labeling. *NMR Biomed.* 2019;32:e4105.
75. Hablitz LM, Vinitzky HS, Sun Q, et al. Increased glymphatic influx is correlated with high EEG delta power and low heart rate in mice under anesthesia. *Sci Adv.* 2019;5:eaav5447.
76. Bèchet NB, Kylkilahti TM, Mattsson B, Petrasova M, Shanbhag NC, Lundgaard I. Light sheet fluorescence microscopy of optically cleared brains for studying the glymphatic system. *J Cereb Blood Flow Metab.* 2020;40:1975-1986.
77. Frey A, Homola GA, Henneges C, et al. Temporal changes in total and hippocampal brain volume and cognitive function in patients with chronic heart failure—The COGNITION.MATTERS-HF cohort study. *Eur Heart J.* 2021;42:1569-1578.
78. Mueller K, Thiel F, Beutner F, et al. Brain damage with heart failure: Cardiac biomarker alterations and gray matter decline. *Circ Res.* 2020;126:750-764.
79. Fultz NE, Bonmassar G, Setsompop K, et al. Coupled electrophysiological, hemodynamic, and cerebrospinal fluid oscillations in human sleep. *Science.* 2019;366:628-631.
80. Jiang-Xie LF, Drieu A, Bhasi K, Quintero D, Smirnov I, Kipnis J. Neuronal dynamics direct cerebrospinal fluid perfusion and brain clearance. *Nature.* 2024;627:157-164.
81. Murdock MH, Yang CY, Sun N, et al. Multisensory gamma stimulation promotes glymphatic clearance of amyloid. *Nature.* 2024;627:149-156.
82. Berridge CW, Waterhouse BD. The locus coeruleus–noradrenergic system: Modulation of behavioral state and state-dependent cognitive processes. *Brain Res Rev.* 2003;42:33-84.
83. Hartupee J, Mann DL. Neurohormonal activation in heart failure with reduced ejection fraction. *Nat Rev Cardiol.* 2017;14:30-38.
84. Cohn JN, Levine TB, Olivari MT, et al. Plasma norepinephrine as a guide to prognosis in patients with chronic congestive heart failure. *N Engl J Med.* 1984;311:819-823.
85. Anand IS, Fisher LD, Chiang YT, et al. Changes in brain natriuretic peptide and norepinephrine over time and mortality and morbidity in the valsartan heart failure trial (Val-HeFT). *Circulation.* 2003;107:1278-1283.
86. Pullen AB, Kain V, Serhan CN, Halade GV. Molecular and cellular differences in cardiac repair of male and female mice. *J Am Heart Assoc.* 2020;9:e015672.
87. Cavaasin MA, Tao Z, Menon S, Yang XP. Gender differences in cardiac function during early remodeling after acute myocardial infarction in mice. *Life Sci.* 2004;75:2181-2192.
88. Giannetto M, Xia M, Stæger FF, et al. Biological sex does not predict glymphatic influx in healthy young, middle aged or old mice. *Sci Rep.* 2020;10:16073.
89. Noll NA, Lal H, Merryman WD. Mouse models of heart failure with preserved or reduced ejection fraction. *Am J Pathol.* 2020;190:1596-1608.
90. Valero-Muñoz M, Backman W, Sam F. Murine models of heart failure with preserved ejection fraction. *JACC Basic Transl Sci.* 2017;2:770-789.
91. Sharma K, Kass DA. Heart failure with preserved ejection fraction: Mechanisms, clinical features, and therapies. *Circ Res.* 2014;115:79-96.
92. Gottschalk M, Swanberg K. kswanberg/rcbFLOW: rcbFLOWv1.0.0. Published online 4 June 2024. <https://doi.org/10.5281/zenodo.11475856>